Stability of a Variable-Speed Permanent Magnet Wind Generator With Weak AC Grids

Nicholas P. W. Strachan, *Member, IEEE*, and Dragan Jovcic, *Senior Member, IEEE*

***Abstract*—The operation of high-power wind generators with weakened ac grids has historically been difficult because of stability and power quality issues. This paper presents an analytical stability study of a variable-speed directly-driven permanently-excited 2-MW wind generator connected to ac grids of widely varying strength and very weak grids. The generator includes two back-to-back full-scale vector controlled 3-level neutral-point-clamped (NPC) voltage-source-converters (VSC). A 47th order small-signal analytical wind generator model is developed within MatLab, and a summary of the model structure and controls is given. Model verification is demonstrated for fast and slow system variables employing detailed simulation software PSCAD/EMTDC. An eigenvalue stability study for weak ac networks is presented, and qualitative conclusions about inherent system dynamics and stability characteristics are given. These insights are employed to study the design of an ac voltage controller for weak ac networks. Two alternative controller designs are studied for their potential to enhance system robustness to changes in ac grid strength. Testing on the detailed simulator PSCAD/EMTDC is employed throughout to confirm conclusions from analytical studies.**

***Index Terms*—Control systems, eigenvalues and eigenfunctions, modeling, permanent-magnet generators, pulsewidth modulated power converters, stability, wind power generation.**

I. Introduction

In RECENT years, strict wind power grid connection requirements have emerged in order to protect future power quality and reliability as wind energy penetration levels markedly increase [1]–[3].

Grid "strength" is a key indicator as to the technical difficulty experienced in meeting these requirements. With "strong", low impedance grid connections at the point of common coupling (PCC), distributed generation has only a limited influence on local bus voltage and therefore power quality/stability [2]. Wind power plants are, however, commonly located in remote areas (best wind resource), where grid impedance is as a result typically high (long feeders) and fault level low. Even with relatively strong networks, grid impedance may change significantly during operation as the result of faults, tripping of lines or load variations. With "weak", high impedance grid connections, load fluctuations can significantly influence local bus voltage, and therefore power quality/stability. Consequently, weak ac grids can pose serious interconnection problems in practice by limiting the amount of wind power that can be integrated [2]. Expensive network reinforcements can therefore sometimes be required.

Whilst it is generally accepted that weak ac grids cause stability and power quality issues, historically this phenomenon has been challenging to study. Studies of interactions between modern wind generator technologies and host grid systems have been generally reported using detailed electromagnetic-transient (EMT) type simulations [4], [5]. These accurately simulate power electronics at the expense of small simulation step sizes and long simulation studies. Furthermore, these software tools support only time-domain trial and error simulations, and as a result can not readily offer qualitative conclusions. Multidimensional design problems are therefore notoriously difficult to study with such methods.

In contrast, and complementing EMT type simulation, analytical small-signal modeling facilitates the use of stability analysis techniques, such as eigenvalue analysis or frequency-domain techniques [6], [7]. This offers invaluable insights into inherent system dynamics and stability characteristics, and allows rapid sensitivity studies to be performed. Development of such models for complex nonlinear systems however requires long mathematical analysis. Furthermore, the resulting models are only accurate around steady-state operating points (small-signal) and PSCAD verification is always required.

The development of analytical models, and the application of stability/control analysis techniques, is widely reported over recent decades in various fields of electrical power engineering [8]–[10]. However, analytical models of, and stability/control analysis studies applied to, modern wind power generators are not yet widely reported. Manufacturers safeguard detailed high-order time-domain and state-space wind generator models due to commercial sensitivity, and only make available reduced order low-frequency models suitable for power flow analysis studies. Such models are inadequate for developing fast and robust wind generator controls.

This paper thus presents firstly, as background, the development of a detailed analytical small-signal model of a variable-speed directly-driven permanently-excited 2-MW wind generator. The small-signal model is then employed to conduct a weak ac grid connection study (employing eigenvalue analysis), with the aim of ultimately improving system robustness to changes in ac grid strength. The methodologies adopted and conclusions made in this study can be similarly applied to other wind generator types/studies. In a broader context therefore, this paper aims to support and stimulate the further development and application of small-signal models to wind power studies specifically.

Manuscript received May 07, 2009; revised February 27, 2010, April 27, 2010, and May 27, 2010; accepted June 09, 2010. Date of current version September 22, 2010. Paper no. TPWRD-00350-2009.

The authors are with University of Aberdeen, School of Engineering, King's College, Aberdeen, AB24 3UE, Scotland. (e-mail: n.p.w.strachan@googlemail.com).

Digital Object Identifier 10.1109/TPWRD.2010.2053723

Studies of directly-driven wind generators have been previously reported in [5], [11] and [12]. However, these studies employ EMT simulation models and do not therefore address analytical modeling of wind generator dynamics. The issue of wind farm interaction with a weak ac grid has been studied in [13]. However this study also employs EMT simulation and is constrained to a large wind farm with HVDC interconnection. The paper is organized as follows. The wind generator test system and controls are summarized in Section II. A controller optimization and system stability study follows in Section III and Section IV respectively, and an analytical stability study of weak ac grid connections is presented in Section V.

II. Test System Modeling

A. Test System

Fig. 1 depicts a schematic representation of the wind generator model. The model consists of a variable-speed wind turbine directly driving a 2-MW permanent magnet (PM) synchronous generator. The PM generator is connected at the PCC to the host power system via a controlled full-scale power converter system (PCS), step-up transformer, and shunt connected high-pass harmonic filter.

The PCS comprises of two back-to-back 3-level neutral-point-clamped (NPC) voltage-source-converters (VSC). Each converter employs subharmonic pulsewidth modulation (PWM) with carrier band phase disposition [14], [15]. Vector control is employed on both sides of the PCS in synchronously rotating reference frames [15]. Key system parameters are detailed in Tables III and IV.

B. Control Structure

Three distinct controllers manage the operation of the wind generator. These are the blade pitch angle (BPA) controller, generator facing controller, and grid facing controller. The BPA controller is responsible for maintaining rated power during excessive wind speeds (above rated), and is therefore excluded from the analytical small-signal model [1], [16].

1) Controller for PM Generator Facing Converter: The generator controller is responsible for optimizing rotor speed in order to continually maximize wind energy capture.

A salient pole PM generator, without damper windings [12], is modeled in a synchronously rotating rotor-aligned dq reference frame as [11], [15]

$$\frac{1}{2}m_{Rd}v_{DCR} = R_S i_{ACRd} + (L_{Md}+L_{LS})\frac{di_{ACRd}}{dt} - \omega_r(L_{Mq}+L_{LS})i_{ACRq} \quad (1)$$

$$\frac{1}{2}m_{Rq}v_{DCR} = R_S i_{ACRq} + (L_{Mq}+L_{LS})\frac{di_{ACRq}}{dt} + \omega_r(L_{Md}+L_{LS})i_{ACRd} + \omega_r\Psi_f \quad (2)$$

$$\frac{d}{dt}\omega_r = \frac{P}{2J}\left(t_M - \frac{3}{2}\frac{P}{2}\left((L_{Md}-L_{Mq})i_{ACRd}+\Psi_f\right)\times i_{ACRq}\right) \quad (3)$$

where d and q denote rectangular frame direct and quadrature components; m_R is the rectifier modulation control signal,

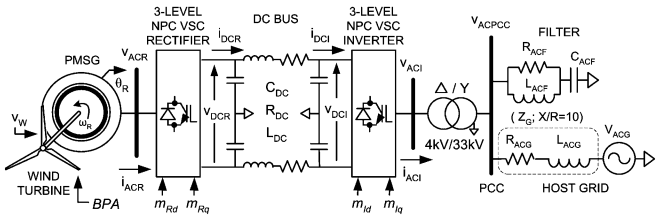

Fig. 1. Wind generator model schematic.

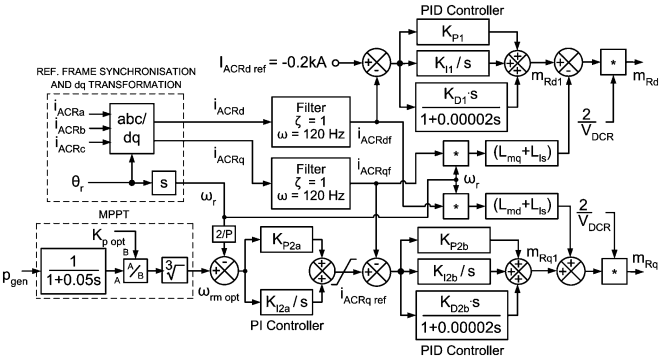

Fig. 2. PM generator facing controller model.

v_{DCR} is the generator-side dc bus voltage, R_S is stator resistance, L_M is mutual inductance, L_{LS} is stator leakage inductance, i_{ACR} is rectifier/stator current, ω_r is rotor electrical speed, Ψ_f is the permanent magnet flux, J is the combined moment of inertia (turbine and rotor), P is the number of machine poles and t_M is the mechanical turbine torque.

Rotor electrical speed (ω_r) in (3), and thus rotor mechanical speed $(\omega_{rm} = 2\omega_r/P)$, is continually controlled in order to maximize turbine aerodynamic efficiency by maintaining an optimal tip speed ratio (TSR) between linear blade tip speed $(\omega_{rm}R)$ and wind speed (V_W), [16]. Rotor speed control is achieved by manipulating the dq stator currents in (1) and (2) to control machine torque in (3). The control signals are the dq components of the rectifier modulation signal (m_{Rd}, m_{Rq}). Rotor speed is ultimately optimized by controlling main synchronous torque in (3) using the quadrature stator current (i_{ACRq}). A 0.2 kA direct current reference $(i_{ACRd\,ref})$ is selected (in combination with increased PM flux excitation) in order to curtail both reactive power and terminal voltage [15].

The complete generator controller schematic is depicted in Fig. 2. Two inner fast proportional-integrator-differential (PID) controllers ensure that the converter currents are bounded under all conditions including ac faults. An optimum speed reference ω_{ropt}, corresponding to maximum power point tracking (MPPT), is derived using an active power measurement. By analyzing the power produced by the wind turbine for various wind speeds, an optimum relationship between generated power and rotor speed is derived [17]. The rotor speed error is processed in an outer cascaded proportional-integral (PI) control loop. A rotor position measurement (θ_r) is used to align and synchronize the dq reference frame.

2) AC Grid Facing Controller: The grid facing controller is responsible for controlling energy exchange between the PCC

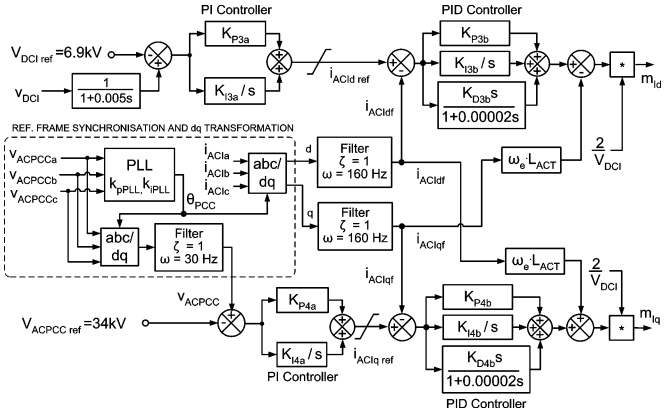

Fig. 3. AC grid facing controller model.

and host power system by controlling active and reactive power at the PCC bus (Fig. 1).

The equations describing the ac circuit linking the inverter and PCC, stated in a dq reference frame synchronously rotating with the PCC ac voltage vector (V_{ACPCC}), are

$$\frac{1}{2}m_{Id}v_{DCI} = v_{ACPCCd} + R_C i_{ACId} - \omega_e L_{ACT} i_{ACIq} + L_{ACT}\frac{d}{dt}i_{ACId} \quad (4)$$

$$\frac{1}{2}m_{Iq}v_{DCI} = v_{ACPCCq} + R_C i_{ACIq} + \omega_e L_{ACT} i_{ACId} + L_{ACT}\frac{d}{dt}i_{ACIq} \quad (5)$$

$$p_{ACPCC} = \frac{3}{2}(v_{ACPCCd}\cdot i_{ACId} + v_{ACPCCq}\cdot i_{ACIq}) \quad (6)$$

$$q_{ACPCC} = \frac{3}{2}(v_{ACPCCq}\cdot i_{ACId} - v_{ACPCCd}\cdot i_{ACIq}) \quad (7)$$

where m_I is the inverter modulation control signal, v_{DCI} is the inverter-side dc voltage, R_C represents converter losses, L_{ACT} is transformer leakage inductance, i_{ACI} is inverter ac current, ω_e is the grid frequency, and P/Q_{ACPCC} is the active and reactive power at the PCC bus.

The inverter-side reference frame is orientated with the PCC voltage vector [using a phase-locked loop (PLL)], such that $v_{ACPCCq} = 0$ and $v_{ACPCCd} = |v_{ACPCC}|$. Consequently, (6) and (7) simplify and active and reactive power is controlled by independently controlling the inverter current vector components (i_{ACId}, i_{ACIq}) using the inverter modulation control signals (m_{Id}, m_{Iq}) [11].

The grid facing controller schematic is depicted in Fig. 3. Two fast inner PID controllers are employed with decoupling compensation in order to control the inverter current components [17]. Two cascaded outer PI control loops provide inner control references corresponding to desired PCC active and reactive power levels.

The active power reference is derived from an inverter-side dc voltage error in order to ensure a "stiff" dc-bus voltage. A "stiff" dc-bus voltage ensures good stability of the generator-facing controller and prevents insulation deterioration. The reactive power set-point is derived from an ac voltage error. Reactive power is thus controlled to maintain a reference PCC voltage (34 kV). The reference corresponds to zero inverter reactive power exchange, and thus permits maximum reactive power contribution during grid fault scenarios.

An accurate PCC voltage vector position (θ_e), for reference frame alignment and synchronization, is obtained using a $D-Q-Z$ type PLL [18]. Note that both ac and dc voltage filtering is employed to eliminate harmonics and ensure system stability.

C. Analytical Model

1) Small-Signal Linear Model: The wind generator system under study includes several highly nonlinear subsystems, including the; mechanical wind turbine model, rectifier/inverter linking converter models, PM machine model, MPPT algorithm/power measurement, and controller decoupling compensation. In order to produce an analytical model that will facilitate the use of eigenvalue control and stability analysis techniques, a linear small-signal model of the complete wind generator system is produced. Only the small-signal approximations of the turbine and converter models are detailed. Remaining elements are linearized in a similar manner.

2) Wind Turbine Model: The torque (t_M) extracted by the turbine from the wind in (3) is a function of the wind speed (v_W), rotor speed (ω_{rm}), and turbine performance coefficient (c_P) according to (where ρ_A is air density and A_R is the turbine swept area) [16]

$$t_M = \frac{0.5\cdot\rho_A\cdot A_R\cdot v_W^3\cdot c_P}{\omega_{rm}.} \quad (8)$$

The performance coefficient (c_P) models the aerodynamic efficiency of the wind turbine numerically as a nonlinear function of the instantaneous TSR and BPA as detailed in [1], [16], [17]. Since the BPA controller is excluded $(\mathrm{BPA} = 0)$, the c_P numerical model simplifies and substitution can be made for TSR $(\omega_{rm}R/V_W)$. Making substitutions into (8) for c_P, ρ_A and A_R ultimately results in a nonlinear mechanical torque expression as a function of wind and rotor speed. Using linearization principles, the ultimate small-signal torque expression is derived (where superscript ^{0} denotes nominal values) as

$$\Delta t_m = \frac{-\mathring{v}_w^2\cdot\left(4057\cdot\mathring{v}_w^2 - 47453\cdot\mathring{v}_w\cdot\mathring{\omega}_{rm} + 86361\cdot\mathring{\omega}_{rm}^2\right)}{\mathring{\omega}_{rm}^3}\cdot e^{\left(\frac{-0.48\cdot\mathring{v}_w}{\mathring{\omega}_{rm}}\right)}\cdot\Delta v_w + \frac{\mathring{v}_w^3\cdot\left(28787\cdot\mathring{\omega}_{rm}^2 - 30696\cdot\mathring{\omega}_{rm}\cdot\mathring{v}_w + 4057\cdot\mathring{v}_w^2\right)}{\mathring{\omega}_{rm}^4}\cdot e^{\left(\frac{-0.48\mathring{v}_w}{\mathring{\omega}_{rm}}\right)}\cdot\frac{2}{P}\cdot\Delta\omega_r. \quad (9)$$

Substituting (9) into (3) for (t_M), results in a final linear small-signal approximation of the equation of motion (assuming linearized machine torque). The test system parameters are given in Tables III and IV.

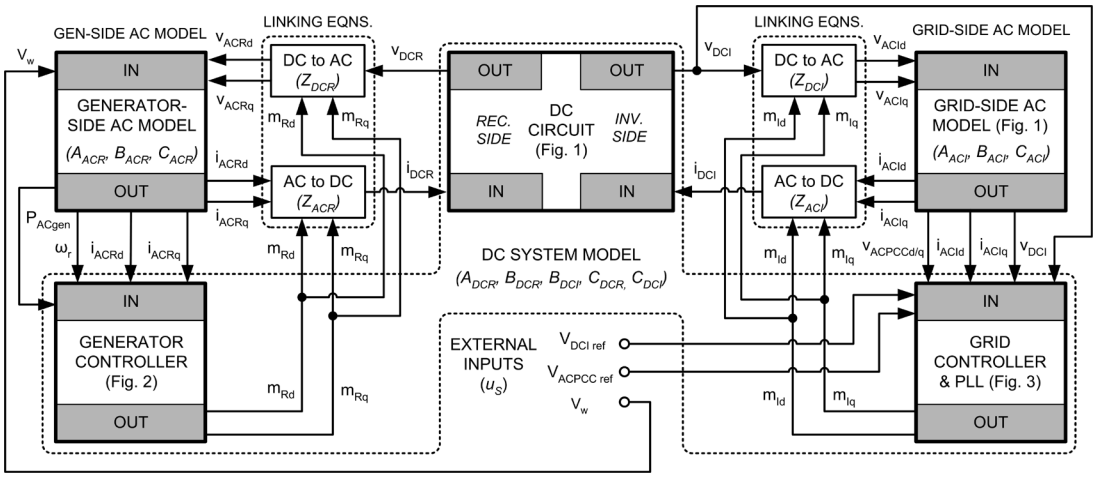

Fig. 4. Analytical wind generator model structure.

3) Converter Models: Linking between dc and ac voltages is achieved with the following linearized fundamental converter equations (either rectifier or inverter subscripts) [18]

$$\Delta v_{ACRd} = \frac{1}{2}\overset{0}{m}_{Rd}\Delta v_{DCR} + \frac{1}{2}\overset{0}{v}_{DCR}\Delta m_{Rd} \tag{10}$$

$$\Delta v_{ACRq} = \frac{1}{2}\overset{0}{m}_{Rq}\Delta v_{DCR} + \frac{1}{2}\overset{0}{v}_{DCR}\Delta m_{Rq}. \tag{11}$$

Linking between ac and dc converter currents is similarly achieved by combining fundamental converter voltage equations, with ac/dc power balance equations, giving

$$\begin{aligned}\Delta i_{DCR} = &-\frac{3}{4}\frac{1}{C_{DCR}}\overset{0}{i}_{ACRd}\Delta m_{R_d} - \frac{3}{4}\frac{1}{C_{DCR}}\overset{0}{i}_{ACRq}\Delta m_{Rq} \\ &-\frac{3}{4}\frac{1}{C_{DCR}}\overset{0}{m}_{Rd}\Delta i_{ACRd} \\ &-\frac{3}{4}\frac{1}{C_{DCR}}\overset{0}{m}_{Rq}\Delta i_{ACRq}.\end{aligned} \tag{12}$$

4) Analytical Model Structure: A 47th order multiple-input multiple-output (MIMO) small-signal model of the wind generator system and controls (Figs. 1–3) is developed in state-space form within MatLab. The model structure is depicted in Fig. 4 and consists of the following three interlinked subsystem state-space models: generator-side ac model (3rd order), dc system model (34th), and grid-side ac model (10th). The subsystem model structure provides the flexibility for a wide range of studies.

The generator-side ac subsystem comprises of the generator and turbine model (Fig. 1). The dc subsystem (enclosed by a broken border) comprises of the generator controller (Fig. 2), dc circuit (Fig. 1), grid controller and PLL model (Fig. 3). The grid-side ac subsystem comprises of the transformer, grid and filter models (Fig. 3).

The coupling between the respective subsystems is achieved using selected variables, with d and q denoting the vector components. The input and output variables of the subsystems are conditioned using linking matrices (Z_{DCR}, Z_{DCI}, Z_{ACR}, Z_{ACI}) that are developed using converter fundamental frequency modeling equations (10)–(12) [18]. The generator equations include the variable speed of the coordinate frame (ω_r) to accommodate modeling at a range of wind speeds. Additional coupling matrices provide the measured and reference variables required by the respective controllers (Figs. 2 and 3).

A master external wind speed input (V_W) allows both mechanical torque in (3) to be derived, and for all nominal values to be calculated. The state-space wind generator model, as depicted in Fig. 4, is written in standard matrix form as

$$\frac{dxs}{dt} = A_s \cdot x_s + B_s \cdot u_s \tag{13}$$

$$y_S = C_S \cdot x_S \tag{14}$$

where the system matrix (A_s) incorporates the subsystem and linking matrices, and the input/output vectors (u_s/y_s) are as shown in (15) and (16), at the bottom of the next page.

III. Controller Optimization

A. Inner Fast Control Loops

The fastest current controllers can be designed using model simplifications. Using (1), and assuming fast dc voltage control ($V_{DCR} = const$), we derive the control signal m_{Rd} to include the PID control signal m_{Rd1} and decoupling compensation as

$$m_{Rd} = 2\frac{(m_{Rd1} - \omega_r(L_{Mq} + L_{LS})i_{ACRq})}{v_{DCR}}. \tag{17}$$

Substitution of (17) into (1) and re-arranging gives

$$\frac{i_{ACRd}}{m_{Rd1}} = \frac{1}{R_s + (L_{Md} + L_{LS})s}. \tag{18}$$

Assuming a negligible stator resistance, (18) represents a dominant integral system. Consequently, a proportional (k_p) and differential (k_d with time constant T_d) controller combines with (18) in a feedback loop to give a second-order system

$$\frac{i_{ACRd}}{i_{ACRdREF}}$$

$$= \frac{(K_p T_d s + k_d)s + k_p}{(L_{Md} + L_{LS})T_d s^2 + (L_{Md} + L_{LS} + K_p T_d s + k_d)s + k_p}. \quad (19)$$

Considering desired speed of response (around 30 ms time const. and damping ratio over 0.7), the parameters k_p, k_d and T_d can be calculated. A small integral gain k_i is also included to eliminate steady-state error caused by nonzero stator resistance R_s. The q-axis controller is designed in same manner using (2), where $\omega_r \Psi_f$ is ignored as slow varying.

The final controller gains are given in Tables III and IV.

B. Outer Controllers

The outer controllers have the frequency bandwidth which is affected by all the subsystems and therefore the complete system model is used. The controller gain optimization is performed by employing the root locus technique using the developed linear small-signal model within MatLab, and latterly confirmed with detailed nonlinear PSCAD simulation.

A PI controller introduces two parameters; the zero $k_z = -k_i/k_p$ and the open-loop gain k_c. The zero is firstly located close to the dominant real pole and then the gain is varied using root locus. Figs. 5 and 6 shows the root locus for dc voltage and ac voltage controllers, respectively, where k_c is varied between 20% and 200%. The dc voltage controller design is clearly more challenging since two pairs of complex poles have long locus branches. The design in Figs. 5 and 6 is also iterative, since the locus in one figure is dependent on the prior selections in the other loop. Fig. 6(c) clearly shows the multivariable coupling between the outer loops.

IV. System Stability

Initial system stability investigations are performed for a base-case grid impedance chosen to correspond to a short circuit ratio ($SCR = PCC\ short\ circuit\ pwr./max.\ apparent\ pwr.\ of\ wind\ generator$[2]) of 10 ($|\mathrm{Zg}| = 44\ \Omega$, $\mathrm{X/R} = 10$). A SCR of 10 is considered in this paper as the boundary below which the host ac system is considered as "weak." It is assumed that systems having $\mathrm{SCR} > 20$ would be strong grids.

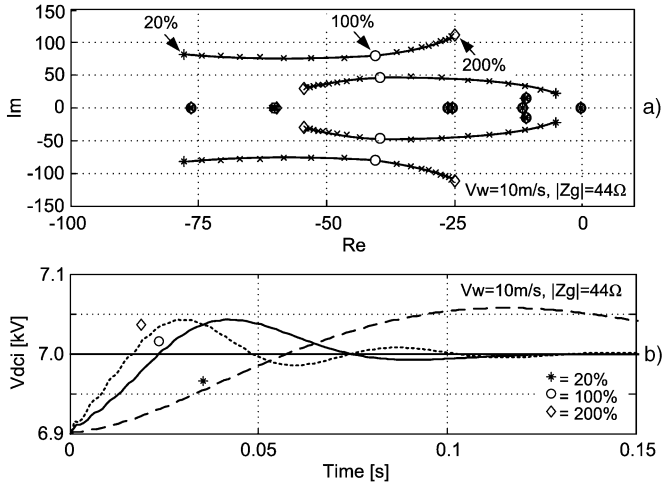

Fig. 5. DC voltage control PI gain ($\mathrm{K_{P3a}}, \mathrm{K_{I3a}}$) optimization ($\mathrm{SCR} = 10$).

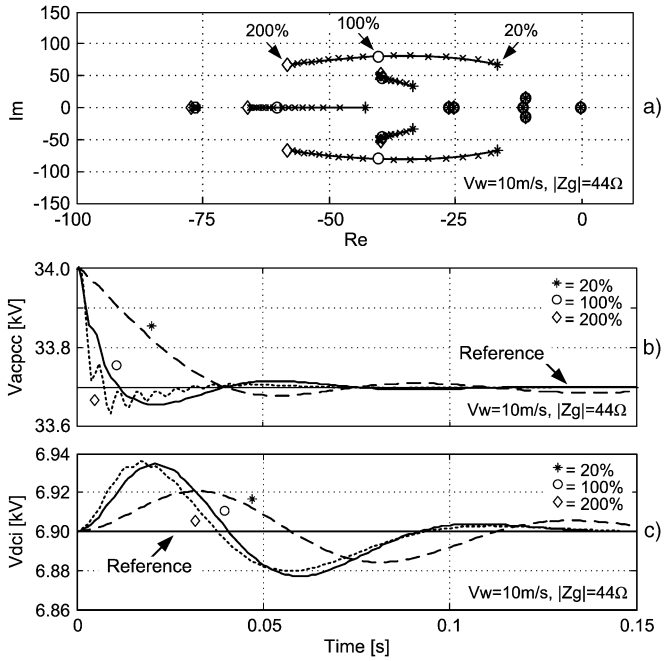

Fig. 6. AC voltage control PI gain ($\mathrm{K_{P4a}}, \mathrm{K_{I4a}}$) optimization ($\mathrm{SCR} = 10$).

A. Model Validation for Fast Dynamics

The studied electromechanical system has dominant slow (mechanical) and fast (electrical) dynamics, and thus analytical model validation is confirmed for a wide range of inputs.

Fig. 7 shows the comparison between the linear small-signal model and detailed nonlinear PSCAD simulation following a +0.1 kV step change in reference dc-bus voltage. Rotor speed (slow dynamics) is only negligibly affected and hence not shown. The PSCAD model responses exhibit greater noise content (owing to detailed converter modeling), however it can be clearly appreciated that the linear small-signal model

$$A_S = \begin{bmatrix} A_{DC} & B_{DCR} \cdot Z_{ACR} \cdot C_{ACR} & B_{DCI} \cdot Z_{ACI} \cdot C_{ACI} \\ B_{ACR} \cdot Z_{DCR} \cdot C_{DCR} & A_{ACR} & 0 \\ B_{ACI} \cdot Z_{DCI} \cdot C_{DCI} & 0 & A_{ACI} \end{bmatrix} \quad (15)$$

$$u_S = \begin{bmatrix} v_W \\ V_{DCI\ ref} \\ V_{ACPCC\ ref} \end{bmatrix} \quad y_S = \begin{bmatrix} p_{gen} \\ v_{DCI} \\ v_{ACPCC} \\ \omega_R \end{bmatrix} \quad (16)$$

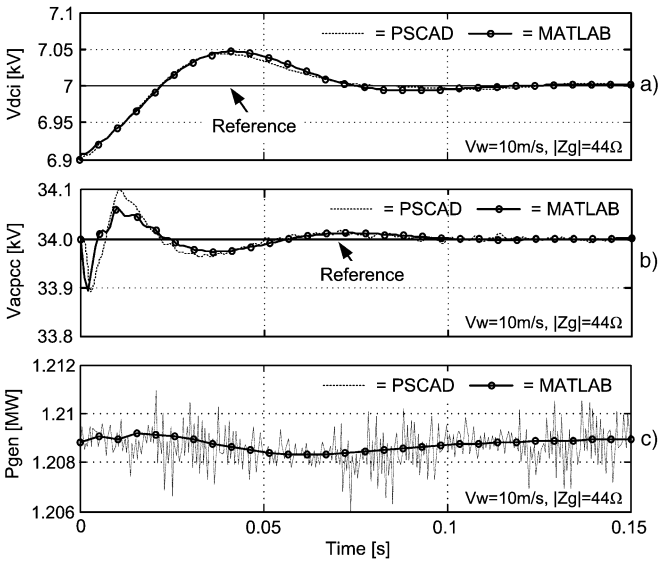

Fig. 7. Analytical model verification against detailed nonlinear simulation following a +0.1-kV dc voltage reference step change (SCR = 10).

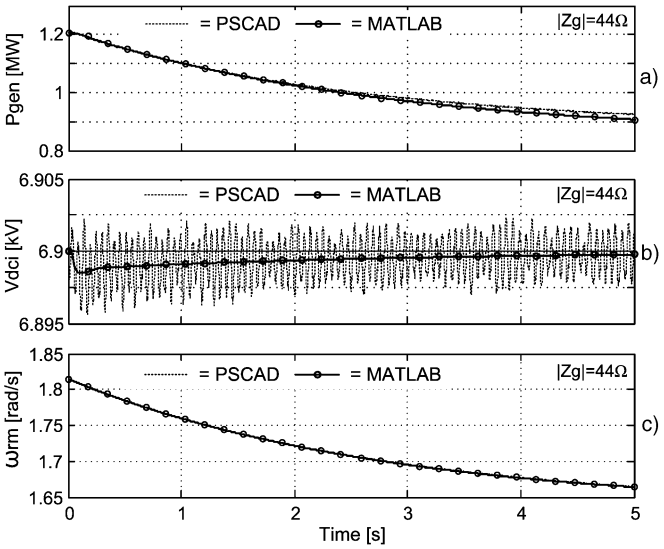

Fig. 8. Analytical model verification against detailed nonlinear simulation following a 1-m/s drop in wind speed (Vw = 10 → 9 m/s, SCR = 10).

demonstrates good accuracy in the fast dynamic range. It is also seen that multivariable properties of the system (control interactions between V_{ACPCC} and V_{DCI}) are modeled accurately.

B. Model Validation for Slow Dynamics

Fig. 8 depicts output variables following a step in wind speed from 10 m/s to 9 m/s. AC voltage is negligibly affected and hence not shown. It can be appreciated that the small-signal model demonstrates good accuracy in the slow mechanical dynamic range. Segregation between generator and grid-side subsystems, caused by the dc bus, can also be appreciated in the negligible dc voltage response [Fig. 8(b)].

C. Eigenvalue Analysis

Accurate analytical modeling facilitates eigenvalue studies that would otherwise not be possible with conventional time-domain modeling approaches [6], [9]. Participation factor (PF) and mode sensitivity studies on dominant eigenvalues provide links between system parameters and time-domain behavior (like the poorly damped oscillating responses).

TABLE I
SYSTEM COMPLEX AND REAL MODES (BELOW 300 Hz), |Zg| = 44 Ω, v_w = 10 m/s

Mode	Eigenvalue	Nat. Freq. [Hz]	Damping [%]	Time Const. [s]
21, 22	-37.0 ± j1412.8	224.9	2.6	
23, 24	-176.4 ± j1262.2	202.8	13.8	
27, 28	-47.9 ± j537.7	85.9	8.9	
29, 30	-125.5 ± j473.8	78.0	25.6	
31, 32	-256.2 ± j319.0	65.1	62.6	
33	-214.1			0.005
34, 35	-194.8 ± j75.8	33.3	93.2	
36, 37	-40.3 ± j80.4	14.3	44.8	
38, 39	-39.6 j46.3	9.7	65.0	
40	-76.6			0.013
41	-60.3			0.017
42, 43	-11.1± j14.3	2.9	61.2	
44	-26.3			0.038
45	-25.4			0.039
46	-11.7			0.085
47	-0.36			2.762

Table I shows all the system modes at frequencies below 300 Hz (higher frequencies have less impact). The complex conjugate pairs of the eigenvalues of the system matrix (15) determine the frequency and damping of the oscillatory system modes, and the real eigenvalues give the aperiodic modes.

The eigenvalues uniquely determine system stability and allow characteristics of poorly damped modes to be identified. However, the relative participations of the state variables in the system modes are required in order to make the connection between stability properties and system structure/parameters [6]. The relative participation (%) of grouped state variables in each mode (identified and labeled in Table I) is presented in respective columns within Table II.

The 47 state variables are subdivided into subsystem models (Fig. 4) and grouped accordingly. State variable groupings are identified numerically in the column titled *states*, and corresponding subsystems are detailed to the left. The magnitudes of the participation factors, obtained from the multiplications of the elements of the right and transposed left eigenvectors (rounded to one decimal point), are scaled so that for each mode all contributing states sum to unity [6], [19].

The dynamic segregation between generator-side and grid-side states caused by the dc bus, as seen previously in Figs. 7 and 8, can also be appreciated by the lack of common modes in Table II. The largest participating state in the slowest of the modes (mode 47) is the mechanical rotor speed, which can be explained by the large combined inertia of the turbine and generator rotor. Only one further grouping, the rotor speed MPPT controller, contributes the remaining 4%.

The impact of specific control loops on the modes can also be studied in Table II. The dc bus voltage and PCC ac voltage controller state groupings contribute to the majority of fast modes (23–24 and 31–41) and thus clearly they have a significant im-

TABLE II
RELATIVE PARTICIPATION [%] OF DOMINANT STATE VARIABLES IN SELECTED MODES

SUBSYSTEM			MODE / STATES	21, 22	23, 24	27, 28	29, 30	31, 32	33	34, 35	36, 37	38, 39	40	41	42, 43	44	45	46	47
DC SYSTEM MODEL	DC Circuit		1-5	92	2	-	-	1	2	1	18	22	1	1	-	-	-	-	-
	Generator Controller (Fig. 2)	I_{ACRd}	6-10	-	-	2	60	-	-	-	-	-	-	-	-	95	-	-	-
		MPPT	11-17	-	-	62	3	-	-	-	-	-	-	-	88	-	99	-	4
	Grid Controller (Fig. 3)	Vdc	18-24	2	20	-	-	37	38	16	38	51	5	14	-	-	-	-	-
		Vacpcc	25-32	1	26	-	-	51	57	78	32	16	18	78	-	-	-	-	-
		PLL	33-34	-	-	-	-	1	-	-	2	4	75	5	-	-	-	100	-
GEN-SIDE AC MODEL	Stator Currents		35-36	-	-	36	37	-	-	-	-	-	-	-	12	5	1	-	-
	Mechanical Rotor Speed		37	-	-	-	-	-	-	-	-	-	-	-	-	-	-	-	96
GRID-SIDE AC MODEL			38-47	5	52	-	-	10	3	5	10	7	1	2	-	-	-	-	-

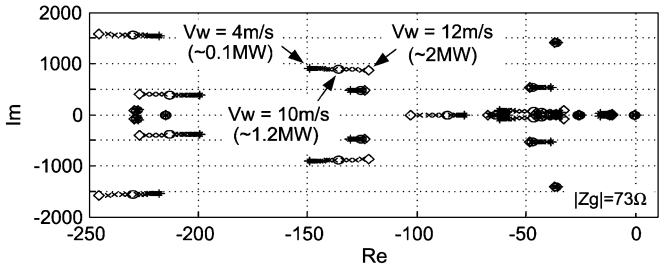

Fig. 9. Root locus for varying operating points between cut-in and rated wind speed ($\mathrm{Vw} = 4 \rightarrow 12\ \mathrm{m/s}$) at a fixed grid strength ($\mathrm{SCR} = 6$).

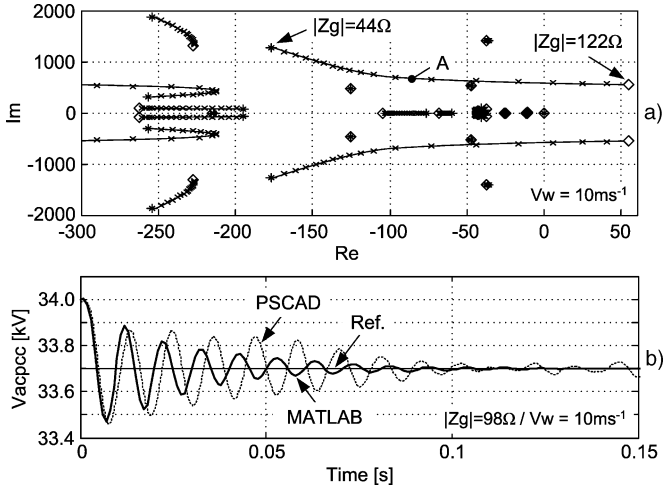

Fig. 10. Grid impedance reduction study: (a) root locus for varying grid strength ($\mathrm{SCR} = 10 \rightarrow 3.5$) and (b) ac voltage step response ($\mathrm{SCR} = 4.5$).

pact on stability. The mode with the lowest damping, 21/22 is associated with the PCS dc circuit.

D. Influence of Operating Point (Wind Speed Changes)

The wind generator frequently changes its operating point as the wind speed fluctuates. A root locus corresponding to a wind speed range between cut-in and rated (4 → 12 m/s) is depicted in Fig. 9. A further "weakened" grid ($\mathrm{SCR} = 6$) is employed since it better illustrates eigenvalue migrations. The 4 m/s operating point is marked by an asterisk ($*$), 10 m/s by a circle (o), and 12 m/s by a diamond ($\Diamond$). It is concluded that the operating point (wind speed) does not significantly affect system dynamics/stability. This relatively insignificant movement of eigenvalues simplifies controller design.

Further analysis is presented for a 10 m/s operating point, which is closer to a practical average wind speed whilst it is also sufficiently below the speed where BPA control activates. Although subsequent analysis is performed at a single wind speed, key conclusions are confirmed by the authors across the full operating wind speed range.

V. STABILITY WITH REDUCED STRENGTH OF AC GRID

A. Grid "Strength" Reduction

Grid strength, in contrast to the operating point, is known to significantly impact system dynamics [2]. The variation of grid parameters is quite common and controllers are expected to ensure good performance across parameter range.

The small-signal model is used to investigate the affect of relative grid strength on the system dynamics. The locus of dominant eigenvalues (assuming controllers are tuned for $\mathrm{SCR} = 10$) for grid impedance variation $44\ \Omega < |\mathrm{Zg}| < 122\ \Omega$ ($3.5 < \mathrm{SCR} < 10$ with fixed $X/R = 10$) is depicted in Fig. 10(a).

A significant sensitivity of system eigenvalues can be seen, with branch A extending into the unstable region at frequencies around 80 Hz. An ac voltage step response using the analytical and PSCAD models near instability ($|\mathrm{Zg}| = 98\ \Omega$, $\mathrm{SCR} = 4.5$) is shown in Fig. 10(b).

Close inspection of the locus [Fig. 10(a)] and Table I reveals that mode 23/24 migrates into the unstable region. Utilizing Table II, it can be seen that the largest of the participating state groupings in mode 23/24, after the grid ac circuit, is associated with the PCC ac voltage controller. This is confirmed by disconnecting the ac voltage controller.

Fig. 11 shows the same grid impedance test [Fig. 10(a)] re-conducted, but with only reactive current control and for an extended grid strength range ($\mathrm{SCR} = 10$ to 1.5). An extended stable operating range, and therefore increased robustness to grid 'strength' variation, can be seen. Reactive current control thus shows better stability than voltage control with weak grids. However, as grid strength decreases (decreasing SCR) voltage control is increasingly desirable in practice in order to reduce PCC power quality issues. Additionally, voltage control

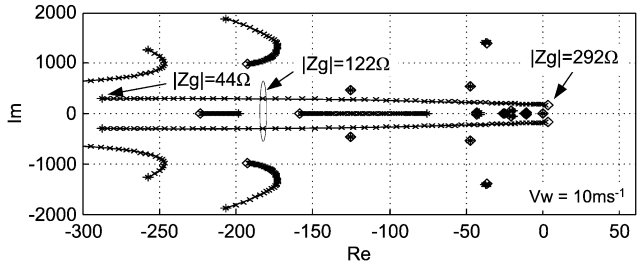

Fig. 11. Root locus for varying grid strength ($\mathrm{SCR} = 10 \rightarrow 1.5$) with no ac voltage control (constant $I_{ACIq\ ref}$).

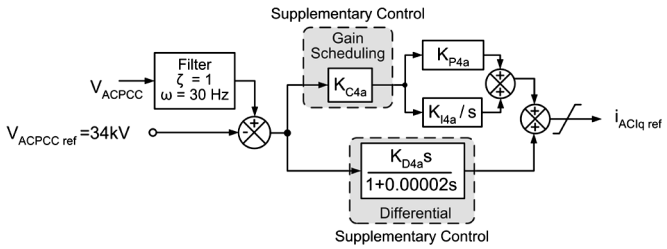

Fig. 12. Weak grid ac voltage supplementary controls.

is desirable in order to assist with fault recoveries [2], and therefore ac voltage control is adopted in our study.

The presented study indicates that the ac voltage controller states significantly impact the unstable eigenvalues. Thus a targeted controller design study, focusing on advanced control methods applied to the PCC ac voltage controller (Fig. 3) is conducted. Two separate control modifications are studied as depicted in Fig. 12, including gain scheduling (K_{C4a}) and additional differential control (K_{D4a}).

B. Adaptive Control (Gain Scheduling)

The locus showing eigenvalue migration for the weak ac grid ($\mathrm{SCR} = 3.5$), assuming gain scheduling from 100% to 25%, is depicted in Fig. 13(a). It is seen that stability is recovered (branch A) by reducing the open loop gain with weak grids. Good performance is now maintained for $|\mathrm{Zg}| = 98\ \Omega$ ($\mathrm{SCR} = 4.5$). The open loop gain would thus ideally be scheduled according to grid strength so to optimize ac voltage control. This control is however difficult to implement since grid strength cannot be readily measured on-line. If a lower, but constant controller gain is adopted for a wide range of grid strength then performance at high grid strength is compromised. Figs. 13(b) and 13(c) show the ac voltage step response for both the original system strength [to contrast with Fig. 6(b)] and for the previous stability boundary [to contrast with Fig. 10(b)] assuming 25% ac voltage gains.

C. Supplementary Differential Control

The root locus for a grid impedance ranging from $|\mathrm{Zg}| = 44\ \Omega$ to $122\ \Omega$ ($\mathrm{SCR} = 10$ to 3.5) with added differential gain (Fig. 12, $K_{D4a} = 15\mathrm{e}-6$) is depicted in Fig. 14(a). It can be seen that system robustness to changes in ac grid strength has been enhanced since branch A is now much shorter, compared with Fig. 10(a). Fig. 14(b) and (c) shows the ac voltage step response for the original system strength [for comparison with Figs. 6(b) and 13(b)] and for the previous stability boundary [for comparison with Figs. 10(b) and 13(c)].

Both system stability and reasonable ac voltage step performance are maintained for a wide range of grid strength. This type of control is relatively simple to implement and may offer the best control solution for connection with weak ac grids. Further PSCAD tests confirm differential ac voltage control is

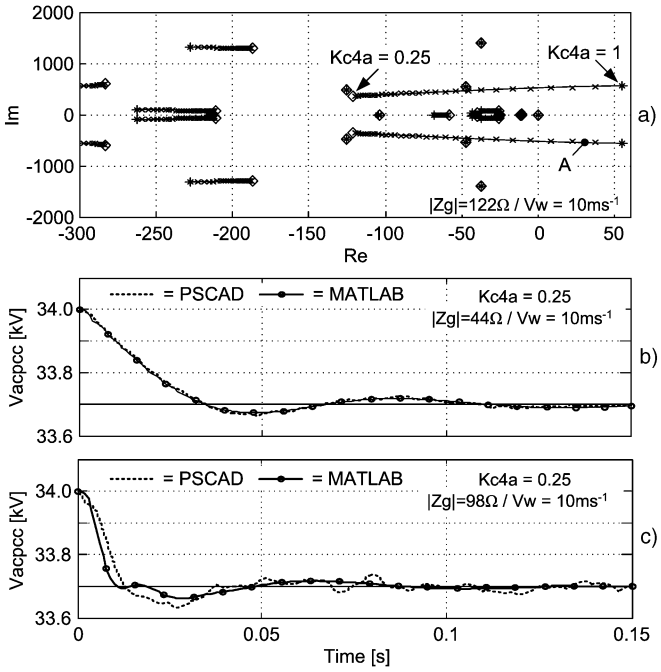

Fig. 13. Gain scheduling study: (a) root locus for $\mathrm{Kc4a} = 100 \rightarrow 25\%$ ($\mathrm{SCR} = 3.5$); (b) ac voltage 0.3 kV reference step response ($\mathrm{SCR} = 10$); and (c) ac voltage 0.3 kV reference step response ($\mathrm{SCR} = 4.5$).

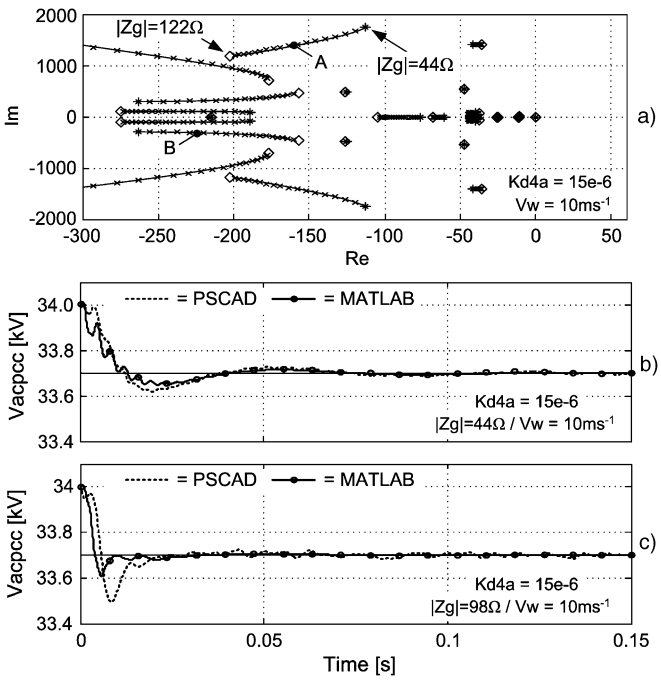

Fig. 14. Differential control study for $\mathrm{Kd4a} = 15\mathrm{e}-6$: (a) root locus for $\mathrm{SCR} = 10 \rightarrow 3.5$; (b) ac voltage 0.3 kV reference step response ($\mathrm{SCR} = 10$); (c) ac voltage 0.3 kV reference step response ($\mathrm{SCR} = 4.5$).

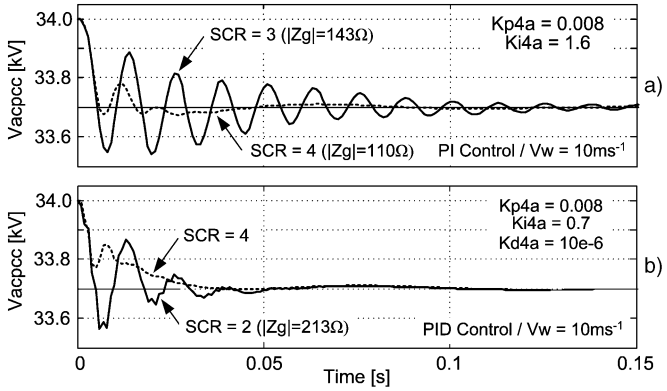

Fig. 15. Robustness testing with nominal ac grid $\mathrm{SCR} = 4$. (a) PI ac voltage controller and (b) voltage controller with supplementary differential feedback.

able to extend the stable operating region to an approximate $\mathrm{SCR} = 4$ before significantly deteriorated step response results and ac voltage gains have to be redesigned. It is noted that filtering is used with the differential term in Fig. 12 in order to reduce high-frequency noise amplification.

D. Very Weak AC Grid

The ac grid strength is further reduced to $\mathrm{SCR} = 4$ and controllers are retuned for best overall performance and robustness. Analytical testing has shown that ac voltage controls can be tuned for reasonable performance at very low SCR, however robustness to further grid changes becomes a significant issue. Fig. 15(a) shows the ac voltage step responses with nominal $\mathrm{SCR} = 4$ and reduced $\mathrm{SCR} = 3$ for simple PI control. It is evident that operation becomes unsatisfactory, even with a modest 25% reduction in grid strength. In Fig. 15(b), the additional differential loop is included (Fig. 12) and it is seen that although performance deteriorates, satisfactory operation may be achieved for a 50% reduction in grid strength.

VI. Conclusions

In this paper, a small-signal 47th-order analytical model for representing permanently-excited directly-driven wind generators is presented. Model verification is demonstrated for both electrical and mechanical system variables, implying that the model is suitable for a wide range of MIMO electromechanical system dynamics studies.

Small-signal stability study shows that grid strength significantly affects system dynamics. By employing participation factor analysis, it is proven that the ac voltage control loop has the most influence on the unstable eigenvalues with weak ac grids. Additional differential control feedback is proposed in order to enhance robustness to grid strength variation. The detailed simulation on PSCAD confirms that supplementary control can significantly extend the stable range for grid strength variation, while maintaining reasonable quality of step responses. A system with nominal $\mathrm{SCR} = 10$ can operate well even if grid strength reduces to $\mathrm{SCR} = 4$, whereas weaker grids tolerate somewhat smaller changes in grid strength. In practice, it will be possible to operate wind generators even with ac systems having $\mathrm{SCR} < 4$ if an advanced ac voltage controller is employed. It is concluded further that the wind speed does not significantly affect system dynamics.

TABLE III
Test System Parameters

Rated Turbine Mech. Power	$P_{M\,rated}$	2MW
Rotor Radius / Air Density	R / ρ	38m / 1.205kg/m3
Max. Cp / Opt. TSR	$C_{P\,MAX}$ / TSR_{OPT}	0.44 / 6.9
Rated Wind / Rotor Speed	$V_{W\,rated}$ / $\omega_{rm\,rated}$	11.8m/s / 2.18rad/s
Opt. Power Coefficient Const.	$K_{P\,OPT}$	0.2008MW/(rad/s)^3
Rated Machine Pwr. / Current	$S_{GEN\ rated}$ / $V_{GEN\ rated}$	2MVa / 0.29kA
Machine Poles / PM Flux	P / Ψ_f	22 / 1.3p.u.
Machine Magnetizing Ind.	X_{Md} / X_{Mq}	1p.u. / 0.65p.u.
Stator Res. / Leakage Ind.	R_S / X_{LS}	0.01p.u. / 0.1p.u.
Gen. + Turbine Inertia Const.	H	3.5sec
Rec. & Inv. Rated Pwr.	$S_{REC\ rated}$ / $S_{INV\ rated}$	2MVa / 2.5MVa
Rec. & Inv. Rated Voltage	$V_{ACR\ rated}$ / $V_{ACI\ rated}$	4kV
Rec. / Inv. Mod. Ratio	$M_{F\,REC}$ / $M_{F\,INV}$	165 / 45
DC Bus Parameters	C_{DC} / L_{DC} / R_{DC}	5mF / 0.0002H / 0.01Ω
Grid Para. (SCR=10, X/R=10)	L_{ACG} / R_{ACG} / V_{ACG}	0.138H / 4.34Ω / 33kV
Transformer Parameters	$S_{T\,rated}$ / L_{ACT}	2.5MVa / 0.15p.u.
Shunt Filter Parameters	C_{ACF} / L_{ACF} / R_{ACF}	2.19uF / 0.016H / 43Ω

TABLE IV
Controller Parameters

K_{P1}	200 1/kA	K_{D2b}	0.02	K_{P4a}	0.01 kA/kV
K_{I1}	5000 1/kAs	K_{P3a}	0.05 kA/kV	K_{I4a}	5 kAs/kV
K_{D1}	0.02	K_{I3a}	2.5 kAs/kV	K_{P4b}	100 1/kA
K_{P2a}	0.01 kA/rad	K_{P3b}	100 1/kA	K_{I4b}	6000 1/kAs
K_{I2a}	0.55 kAs/rad	K_{I3b}	6000 1/kAs	K_{D4b}	0.25
K_{P2b}	200 1/kA	K_{D3b}	0.25	K_{Ppll}	80
K_{I2b}	5000 1/kAs	-	-	K_{Ipll}	800

References

[1] J. G. Slootweg, S. W. H. De Haan, H. Polinder, and W. L. Kling, "General model for representing variable speed wind turbines in power system dynamics simulations," *IEEE Trans. Power Syst.*, vol. 8, no. 1, pp. 144–151, Feb. 2003.

[2] T. Ackermann, *Wind Power in Power Systems*. Chichester, U.K.: Wiley, 2005.

[3] D. Jovcic, "Interconnecting offshore wind farms using multiterminal VSC-based HVDC," in *Proc. IEEE Power Eng. Soc. General Meet.*, Montreal, QC, Canada, Jun. 2006, 7pp.

[4] *PSCAD/EMTDC User's Guide*. Winnipeg, MB, Canada: Manitoba HVDC Research Centre, 2004, ch. 1.

[5] S.-K. Kim and E.-S. Kim, "PSCAD/EMTDC-based modeling and analysis of a gearless variable speed wind turbine," *IEEE Trans. Energy Convers.*, vol. 22, no. 2, pp. 421–430, Jun. 2007.

[6] P. Kundur, *Power System Stability and Control*. London, U.K.: McGraw-Hill, 1994, ch. 12.

[7] S. Skogestad and I. Postlethwaite, *Multivariable Feedback Control: Analysis and Design*. Chichester, U.K.: Wiley, 1996, ch. 11.

[8] R. J. Piwko, H. A. Othman, O. A. Alvarez, and C.-Y. Wu, "Eigenvalue and frequency-domain analysis of the intermountain power project and the WSCC network," *IEEE Trans. Power Syst.*, vol. 6, no. 1, pp. 238–244, Feb. 1991.

[9] D. Jovcic, N. Pahalawaththa, and M. Zavahir, "Small signal analysis of HVDC-HVAC interactions," *IEEE Trans. Power Del.*, vol. 14, no. 2, pp. 525–530, Apr. 1999.

[10] A. R. Wood and C. M. Osauskas, "A linear frequency-domain model of a STATCOM," *IEEE Trans. Power Del.*, vol. 19, no. 3, pp. 1410–1418, Jul. 2004.

[11] M. Chinchilla, S. Arnaltes, and J. C. Burgos, "Control of permanent-magnet generators applied to variable-speed wind-energy systems connected to the grid," *IEEE Trans. Energy Convers.*, vol. 21, no. 1, pp. 130–135, Mar. 2006.

[12] A. Yazdani and R. Iravani, "A neutral-point clamped converter system for direct-drive variable-speed wind power unit," *IEEE Trans. Energy Convers.*, vol. 21, no. 2, pp. 596–607, Jun. 2006.

[13] X. I. Koutiva, T. D. Vrionis, N. A. Vovos, and G. B. Giannakopoulos, "Optimal integration of an offshore wind farm to a weak AC grid," *IEEE Trans. Power Del.*, vol. 21, no. 2, pp. 987–994, Apr. 2006.
[14] D. G. Holmes and T. A. Lipo, *Pulse Width Modulation for Power Converters: Principles and Practice*. New York: IEEE Press, 2003.
[15] B. K. Bose, *Modern Power Electronics and AC Drives*. Upper Saddle River, NJ: Prentice-Hall, 2001.
[16] S. Heier, *Grid Integration of Wind Energy Conversion Systems*. Chichester, U.K.: Wiley, 1998, ch. 2.
[17] N. Strachan and D. Jovcic, "Smoothing wind power fluctuations in an integrated wind energy conversion and storage system (WECSS)," in *Proc. IEEE Power Eng. Soc. General Meet.*, Pittsburgh, PA, Jul. 2008, 8pp.
[18] D. Jovcic, N. Pahalawaththa, and M. Zavahir, "Analytical modelling of HVDC-HVAC interactions," *IEEE Trans. Power Del.*, vol. 14, no. 2, pp. 506–511, Apr. 1999.
[19] P. W. Sauer and M. A. Pai, *Power System Dynamics and Stability*. Upper Saddle River, NJ: Prentice-Hall, 1998.

Nicholas P. W. Strachan (M'05) received the Master's degree (Hons.) and Ph.D. degree in electronic engineering from the University of Aberdeen, Aberdeeen, Scotland, in 2003 and 2010, respectively.

Previously, he was a Control and Instrumentation Engineer in the U.K. oil and gas industry during 2003–2005. His current research interests are wind power generation, electrical energy storage, and control systems.

Dragan Jovcic (S'97–M'00–SM'06) received the Dipl. Eng. degree in control engineering from the University of Belgrade, Belgrade, Yugoslavia in 1993 and the Ph.D. degree in electrical engineering from the University of Auckland, Auckland, New Zealand, in 1999.

He is currently a Senior Lecturer with the University of Aberdeen, Aberdeen, Scotland, where he has been since 2004. He was a Lecturer with the University of Ulster during 2000–2004 and a Design Engineer in the New Zealand power industry during 1999–2000. His research interests lie in FACTS, HVDC, integration of renewable sources, and control systems.